Mechanism and Prediction of Hydrogen Embrittlement in fcc Stainless Steels and High Entropy Alloys

Xiao Zhou,[1,*] Ali Tehranchi,[2] and William A. Curtin[1]
[1]*Laboratory for Multiscale Mechanics Modeling, EPFL, CH-1015 Lausanne, Switzerland*
[2]*Max-Planck-Institut für Eisenforschung GmbH, D-40237 Düssseldorf, Germany*

(Received 6 January 2021; revised 1 July 2021; accepted 6 July 2021; published 19 October 2021)

The urgent need for clean energy coupled with the exceptional promise of hydrogen (H) as a clean fuel is driving development of new metals resistant to hydrogen embrittlement. Experiments on new fcc high entropy alloys present a paradox: these alloys absorb more H than Ni or SS304 (austenitic 304 stainless steel) while being more resistant to embrittlement. Here, a new theory of embrittlement in fcc metals is presented based on the role of H in driving an intrinsic ductile-to-brittle transition at a crack tip. The theory quantitatively predicts the H concentration at which a transition to embrittlement occurs in good agreement with experiments for SS304, SS316L, CoCrNi, CoNiV, CoCrFeNi, and CoCrFeMnNi. The theory rationalizes why CoNiV is the alloy most resistant to embrittlement and why SS316L is more resistant than the high entropy alloys CoCrFeNi and CoCrFeMnNi, which opens a path for the computationally guided discovery of new embrittlement-resistant alloys.

DOI: 10.1103/PhysRevLett.127.175501

Hydrogen embrittlement (HE) in metals has long been a persistent problem [1], causing loss of toughness and ductility and restricting applications. As hydrogen emerges as the best renewable fuel, the need to understand the mechanisms of HE and to develop new structural alloys resistant to this dangerous degradation process are of high importance. Unfortunately, there remains widespread controversy about the physical mechanisms of HE [2–4], and no theory quantitatively predicts embrittlement or its dependence on alloying. This is inhibiting the discovery of new HE-resistant alloys. However, recent reports show that high entropy alloys (HEAs) in the Co-Cr-Fe-Mn-Ni-V family are more resistant to HE than Ni and SS304 (austenitic 304 stainless steel) even while absorbing similar or greater amounts of H under the same charging conditions [5–9]. HEAs are essentially random crystalline alloys consisting of multiple components, all at nondilute concentrations. They can have impressive yield strengths, ductility, and/or fracture toughness [10]. With the recent findings, HEAs thus hold promise for applications in H environments. However, since the origins of HE are largely unknown and embrittlement unpredictable, new principles are needed to design better alloys. Here, we present a theory of embrittlement in fcc metals and alloys that predicts the onset of HE as a function of H concentration across all the HEAs studied to date plus the well-studied 304 and 316L stainless steels (SS304: $Fe_{74}Ni_7Cr_{19}$; SS316L: $Fe_{70}Ni_{12}Cr_{18}$). The theory will enable computationally guided searches for new alloys with even better HE resistance.

Our model for understanding embrittlement begins with the idea that H-free metals are ductile because they are intrinsically ductile: a sharp crack tip will emit dislocations and blunt rather than propagate by cleavage. Crack-tip blunting enables higher loads, further emission, further blunting, and eventually failure by nucleation, growth, and coalescence of voids ahead of the blunted crack [11], with high energy dissipation and high fracture toughness. In the presence of sufficient H, dislocation emission and blunting are prevented and a sharp crack propagates in a brittle cleavage mode. Dislocation plasticity is still present around the crack tip, and crack-tip and dislocation interactions can still generate plasticity [12], but the absence of blunting limits the energy dissipation to levels far lower than that achieved in the ductile failure mode. This transition to cleavage is revealed experimentally in microbeam fracture experiments where cracks that blunt in the absence of H remain very sharp in the presence of H even though dislocation plasticity remains around the sharp crack [13].

Quantitatively, this embrittlement transition is determined by two critical stress intensities at the crack tip: K_{Ic} for brittle cleavage and K_{Ie} for dislocation emission. Note that these are not the much larger macroscopic *applied* values due to (nonblunting) plasticity around the crack. Cleavage is controlled by the fracture free energy γ^F with $K_{\mathrm{Ic}} = \sqrt{\alpha(C)\gamma^F}$ [14] with $\alpha(C)$ an anisotropic elastic coefficient. Dislocation emission is controlled mainly by the unstable stacking fault energy γ^{usf} for slip [15] with $K_{\mathrm{Ie}} = \sqrt{\beta(C)\gamma^{\mathrm{usf}}}$ with $\beta(C)$ another anisotropic elastic coefficient; corrections due to step energy [16] are small for relevant H concentrations. Metals are normally intrinsically ductile because $K_{\mathrm{Ie}} < K_{\mathrm{Ic}}$. The introduction of H, and its diffusion and aggregation at a sharp crack as driven by the crack-tip stresses, decreases γ^F and

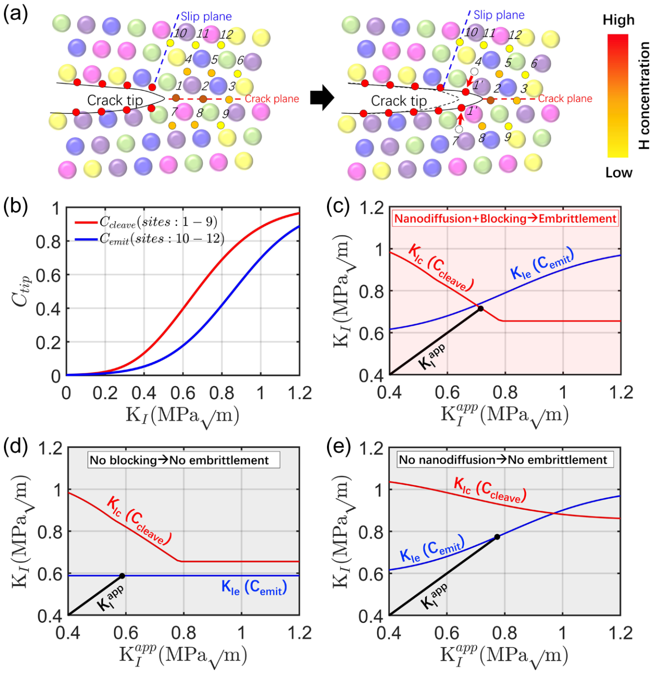

FIG. 1. Mechanism of HE in complex alloys. (a) Schematic of embrittlement process at the crack tip (small spheres: "columns" of H atoms with colors indicating the projected H concentration). Embrittlement occurs because H in sites 4 and 7 "nano" diffuses to the newly created crack surface, increasing the surface H concentration and decreasing the fracture energy, while H in sites 10 and 11 blocks dislocation emission. (b) Schematic of the crack tip H concentrations C_{cleave} and C_{emit} that control embrittlement as a function of K_I^{app} (computed for SS304 at bulk H concentration $C_b = 2600$ at.ppm , $\text{T} = 300$ K). (c) Predicted embrittlement (in SS304, $\text{T} = 300$ K) due to nanodiffusion and blocking of dislocation emission: K_I^{app} (black) reaches K_{Ic} (red) prior to reaching K_{Ie} (blue). (d),(e) Embrittlement is not predicted in the absence of blocking emission or in the absence of nanodiffusion [in both cases, K_I^{app} (black) reaches K_{Ie} (blue) prior to reaching K_{Ic} (red)].

K_{Ic} and increases γ^{usf} and K_{Ie}. At a critical H concentration, $K_{\text{Ic}} < K_{\text{Ie}}$ and a transition to brittle behavior occurs.

The detailed embrittlement processes are shown in Fig. 1(a). H in the bulk lattice at concentration C_b diffuses to the crack-tip region due to the energetic driving force $-p\Delta V$, where p is the pressure field around the sharp crack at the applied stress intensity factor K_I^{app} and ΔV is the misfit volume of interstitial H in the lattice. As K_I^{app} increases, the H concentrations c_i at the various columns i of interstitial sites around the crack tip increase. Cleavage becomes easier due to a reduction in fracture energy that is crucially facilitated by one-atomic-hop H nanodiffusion from the subsurface layers to the new fracture surface [Fig. 1(a) [17]]. The crack-tip H concentration controlling cleavage is $C_{\text{cleave}} = \frac{1}{9}\sum_{i=1}^{9} c_i$, which, after nanodiffusion, leads to two final fracture surfaces with concentrations C_S of one half the concentration on the precracked crack plane plus one half the concentration on each subsurface layer, $C_S = \frac{1}{2}(\frac{1}{3}\sum_{i=1}^{3} c_i) + (\frac{1}{6}\sum_{i=4}^{9} c_i)$ up to $C_{\text{cleave}} = \frac{2}{3}$ and $C_S = 1$ thereafter. H atoms remain in sites further away [sites 10–12 in Fig. 1(a)] at concentration $C_{\text{emit}} = \frac{1}{3}\sum_{i=10}^{12} c_i$, increasing γ^{usf} and K_{Ie} to inhibit dislocation emission (see Fig. S5 in the Supplemental Material [18]) [39,40].

At bulk H concentration C_b, increasing K_I^{app} increases both C_{cleave} and C_{emit} [Fig. 1(b)]. Embrittlement is predicted if K_I^{app} reaches K_{Ic} prior to reaching K_{Ie}. This is best shown by presenting K_{Ic}, K_{Ie}, and K_I^{app} itself versus K_I^{app}. If the line for K_I^{app} first intersects K_{Ie}, the metal is not embrittled and if it first intersects K_{Ic}, the alloy is embrittled [Fig. 1(c)]. Both inhibition of emission and enhancement of cleavage via nanodiffusion are necessary; embrittlement is not obtained if either process is neglected [Figs. 1(d) and 1(e)]. Embrittlement initiates crack growth, which proceeds slowly as H diffuses to the crack and, ultimately, dynamically [41]. Here, we establish conditions for starting crack growth under the accepted assumption that H transport kinetics at room temperature is fast enough to achieve equilibrium at the crack tip [42,43].

Prediction of embrittlement in an alloy requires the bulk concentration C_b, the distribution of H absorption energies in the bulk interstitial sites, the H concentrations C_{cleave} and C_{emit} at the crack tip as a function of K_I^{app}, the fracture free energy γ^F as a function of C_{cleave}, and the unstable stacking fault energy γ^{usf} as a function of C_{emit}. The H absorption energies E_{ab} in a complex alloy depend on the local atomic environments and so are statistically distributed and well-described by a Gaussian density of states $n(E_{\text{ab}}) = (1/\sigma\sqrt{\pi})\exp\{-[(E_{\text{ab}} - \bar{E})/\sigma]^2\}$ with mean $\bar{E}$ and standard deviation σ [Fig. 2(a)]. Migration of H to the crack tip is driven by the applied stress intensity K_I^{app}, which shifts the H absorption energy at interstitial column i at position (r_i, θ_i) relative to the crack tip from E_{ab} to $E_{\text{ab}} - p_i\Delta V$, where $p_i(r_i, \theta_i) = [2(1+\nu)K_I^{\text{app}}/3\sqrt{2\pi r_i}]\cos(\theta_i/2)$ is the pressure at column i. The H concentration c_i in column i is then

$$c_i = \int_{-\infty}^{+\infty} \frac{n(E_{\text{ab}})dE_{\text{ab}}}{1 + \exp\left(\frac{E_{\text{ab}} - p_i\Delta V + E_{\text{ZP}} - \mu}{k\text{T}}\right)}, \qquad (1)$$

where E_{ZP} is the H zero-point energy, k is Boltzmann's constant, T is temperature, and μ the H chemical potential. The critical quantities C_{cleave} and C_{emit} are then computed from the c_i. The bulk concentration C_b can be obtained by setting $p_i = 0$, but here we use the experimentally measured H concentrations C_b^{expt} and embrittlement will depend only on σ and not $\bar{E}$. A single misfit volume $\Delta V = 2.8$ Å^3 is used for all alloys (see Sec. 3 in the Supplemental Material).

The fracture free energy $\gamma^F = \gamma^E + \gamma^S$ includes the creation of a new surface and changes in both energy

(a)

Alloy	**SS304**	**SS316L**	**CoCrNi**	**CoNiV**	**CoCrFeNi**	**CoCrFeMnNi**
C_{11}(GPa)	205	207	252	251	219	196
C_{12}(GPa)	138	135	158	173	126	118
C_{44}(GPa)	126	130	142	109	130	129
α(GPa)	234	241	278	233	252	237
β(GPa)	221	228	265	224	241	225
σ(eV)	0.057	0.102	0.056	0.083	0.069	0.073
$\bar{E}$(eV)	0.077	0.008	0.046	-0.022	0.066	-0.016

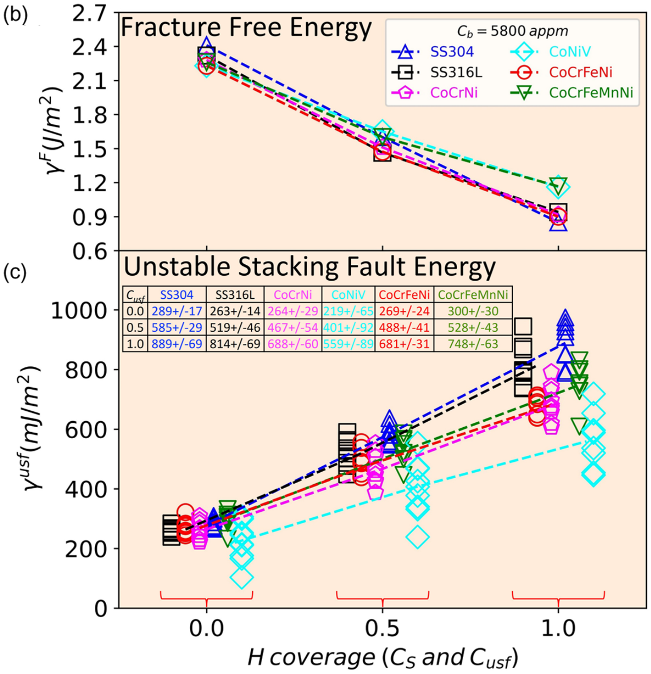

C_{usf}	SS304	SS316L	CoCrNi	CoNiV	CoCrFeNi	CoCrFeMnNi
0.0	289+/-17	263+/-14	264+/-29	219+/-65	269+/-24	300+/-30
0.5	585+/-29	519+/-46	467+/-54	401+/-92	488+/-41	528+/-43
1.0	889+/-69	814+/-69	688+/-60	559+/-89	681+/-31	748+/-63

FIG. 2. (a) Alloy elastic constants, anisotropic elastic coefficients, and mean $\bar{E}$ and standard deviation σ of the bulk H absorption energy distribution. (b) γ^F at surface coverage $C_S = 0\%$, 50%, 100% on the (111) surface for $C_b = 5800$ at. ppm. (c) γ^{usf} at fault coverage $C_{\mathrm{usf}} = 0\%$, 50%, 100% on the (111) slip plane on an area of 108 Å^2; the mean values $\bar{\gamma}^{\mathrm{usf}}$ and standard deviations $\sigma_{\mathrm{usf}}^{\mathrm{DFT}}$ are shown.

and entropy upon moving H atoms from the bulk to the surface [17]. The energetic contribution γ^E is calculated for the thermodynamic occupation of the surface sites at surface concentrations $C_S = 0\%$, 50%, 100%. The entropic contribution is $\gamma^S = (k\mathrm{T}/A_0)[-C_S \ln C_b + (1 - C_S)\ln(1 - C_S) + C_S \ln C_S]$, where A_0 is the area per (111) surface site. γ^S is dominated by the bulk H concentration $C_b \ll 1$ because the crack-tip concentration is $C_S \approx 1$. γ^F is converted into K_{Ic} using experimental or discrete Fourier transform (DFT) elastic constants (see Table S1 in the Supplemental Material). The fracture free energies for all alloys are shown in Fig. 2(a) at $C_b = 5800$ at. ppm. Trends are similar, but SS304 shows the largest decrease and CoNiV and CoCrFeMnNi the smallest decreases. CoCrFeMnNi is not the most HE-resistant alloy, however, because fracture free energy is not the only factor.

The DFT-computed unstable stacking fault energy γ^{usf} at coverages $C_{\mathrm{usf}} = 0\%$, 50%, 100% on the (111) slip plane for all alloys is shown in Fig. 2(b). γ^{usf} increases significantly with H concentration—even modest H aggregation deters crack-tip dislocation emission. Values of γ^{usf} at 0% are quite similar except for CoNiV, which is much lower and will emerge as the most HE-resistant alloy. The rate of increase with H is highest for SS304, indicating a greater tendency toward embrittlement, and lowest for CoNiV, again indicating HE resistance. Dislocation nucleation is a local instability that can be triggered by local γ^{usf} fluctuations over the typical area A of the transition state dislocation loop. Local fluctuations that increase γ^{usf} and K_{Ie} deter emission, and so emission will occur elsewhere in local regions at or below the mean; the mean K_{Ie} is thus an upper limit for emission. Local fluctuations that decrease γ^{usf} and K_{Ie} locally can enable dislocation nucleation at loads below the mean value of K_{Ie}. We estimate a lower limit for emission as K_{Ie} calculated at $\bar{\gamma}^{\mathrm{usf}} - \sigma_{\mathrm{usf}}$ over an estimated loop area of $A = {\sim}50$ Å^2 with $\sigma_{\mathrm{usf}} = \sigma_{\mathrm{usf}}^{\mathrm{DFT}}\sqrt{108/50}$ (see Sec. 5 in the Supplemental Material).

We now make predictions of embrittlement and compare them to experiments for all alloys across the experimental concentrations C_b^{expt} that span the embrittlement transition. Predictions for all literature experiments at higher (embrittled) and lower (not embrittled) C_b^{expt} are shown in Figs. S7 and S8 in the Supplemental Material. Recalling Fig. 1(c), embrittlement is predicted if K_I^{app} first intersects K_{Ic}. Figure 3 shows the predictions K_{Ic} and K_{Ie}, and the embrittlement condition $K_I^{\mathrm{app}} = K_{\mathrm{Ic}}$ or $K_I^{\mathrm{app}} = K_{\mathrm{Ie}}$ is indicated by the black dot.

SS304 is the most easily embrittled among all the alloys shown in Fig. 3, as observed in many experiments for $C_b^{\mathrm{expt}} \geq 1900$ at. ppm and not observed for $C_b^{\mathrm{expt}} \leq 1200$ at. ppm [44–48]. Our predictions agree well with experiments, and we highlight the relatively sharp nature of the transition versus C_b as seen experimentally, which is a natural feature of the theory. The relative ease of embrittlement in SS304 is a combination of its relatively large decrease in γ^F [Fig. 2(b)] and relatively large increase in γ^{usf} with increasing C_b [Fig. 2(c)]. However, in the same SS304 embrittled at $C_b^{\mathrm{expt}} = 4000$ at. ppm at T = 300 K, Caskey [44,45] reported no embrittlement at T = 400 K. Changing only the temperature, our theory predicts this shift to no embrittlement at 400 K (Fig. 3). Embrittlement is suppressed at higher T due to the need for larger driving forces to aggregate H at the crack tip and the increased entropic cost in the fracture free energy.

The SS316L alloy is far more resistant to embrittlement (Fig. 3) [6,49,50]. Many experiments show no embrittlement up to the highest bulk concentration $C_b^{\mathrm{expt}} = 7400$ at. ppm [49] studied, and the theory predicts no embrittlement up to this concentration. Inconsistent with all other experiments and thus in question, Zhao *et al.* report embrittlement at $C_b^{\mathrm{expt}} = 2200$ at. ppm (see Fig. S7 in the Supplemental Material) [8]. Embrittlement in

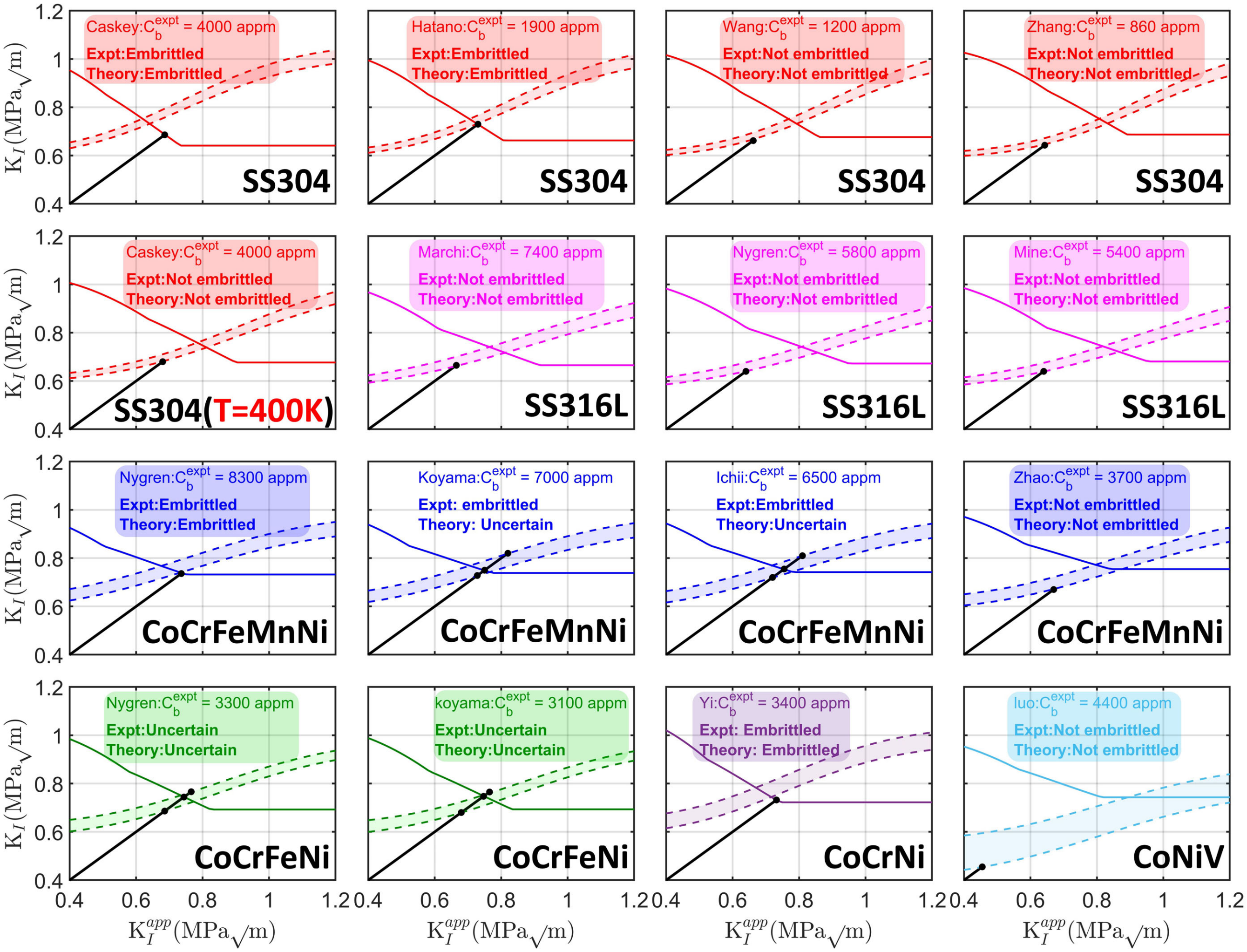

FIG. 3. Embrittlement predictions for fcc alloys. Critical stress intensities K_{Ic}, K_{Ie} (upper, lower limits) as a function of K_I^{app} for all alloys studied, as predicted using the experimentally reported bulk H concentration C_b^{expt}. Theory predictions are determined by the black dot—embrittled if $K_I^{\mathrm{app}} = K_{\mathrm{Ic}}$ first, not embrittled if $K_I^{\mathrm{app}} = K_{\mathrm{Ie}}$ first—and uncertain (three dots shown) if the intersection of $K_I^{\mathrm{app}} = K_{\mathrm{Ic}}$ lies in between the upper and lower K_{Ie}. Experimental observations of embrittlement are stated, and cases where theory and experiment agree are highlighted by shading of the legend.

SS316L is difficult because of the broad distribution of H energies in the bulk such that H is trapped in lower energy sites and thus higher loads are required to drive H to the crack tip.

The HEA CoCrFeMnNi is slightly more susceptible to embrittlement than SS316L (Fig. 3). Nygren *et al.* [5], Koyama *et al.* [51], and Ichii *et al.* [52] all report embrittlement in the range $C_b^{\mathrm{expt}} = 6500$–$8300$ at. ppm. Embrittlement is predicted at 8300 at. ppm, while at the two slightly lower concentrations embrittlement is predicted using the upper limit of K_{Ie} but not the lower limit. Experiments at all lower concentrations ($C_b^{\mathrm{expt}} \leq 3700$ at. ppm) are all observed and predicted to be not embrittled [8,53]. The theory thus captures embrittlement in CoCrFeMnNi well.

For the HEA CoCrFeNi, only two experiments exist in a narrow range $C_b^{\mathrm{expt}} = 3100$–$3300$ at. ppm and report different results, making experiments uncertain in this range (Fig. 3). Specifically, Nygren *et al.* [54] and Koyama *et al.* [55] both reported no reduction of failure strain, which is the main hallmark of embrittlement, but they also report some cleavage fracture surface morphology. These observations suggest that the experiments are around the embrittlement threshold. This is consistent with theory, which predicts no embrittlement at the lower limit of K_{Ie} but embrittlement at the upper limit of K_{Ie}. We note that Koyama also reports no embrittlement at 3600 at. ppm in an alloy with much smaller grain size (2 μm vs 170 μm) [55] (see Fig. S8 in the Supplemental Material). This further suggests that these concentrations are around the transition regime such that embrittlement can depend on additional features such as grain size. Further experiments are needed, but we predict an unambiguous transition to embrittlement at $C_b^{\mathrm{expt}} \sim 5000$ at. ppm.

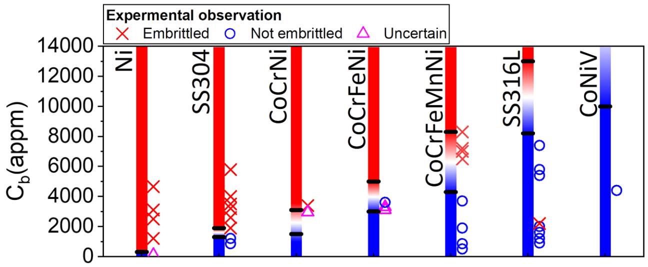

FIG. 4. Predicted embrittled (red) and unembrittled (blue) domains of H concentration for six alloys and Ni along with experimental findings. The transition region corresponding to the upper and lower limits of K_{Ie} is indicated by the thick black lines.

A new experiment on CoCrNi reports embrittlement at $C_b^{\mathrm{expt}} = 3400$ at. ppm [56], which agrees very well with our prediction at this concentration. In our prediction, the unambiguous threshold for embrittlement is at $C_b^{\mathrm{expt}} = 3100$ at. ppm via the lower limit of K_{Ie}. Earlier electrochemically charged CoCrNi at $C_b^{\mathrm{expt}} = 3000$ at. ppm reported an embrittled surface layer and ductile interior [57], indicating an inhomogeneous H distribution for which the theory is not applicable.

One experiment on electrochemically charged CoNiV at the higher concentration $C_b^{\mathrm{expt}} = 4400$ at. ppm shows no embrittlement (Fig. 3), with very high ductility and ultimate strength [58]. We predict CoNiV to clearly be in the ductile regime, consistent with experiments, so that any possible H inhomogeneity would not be important. CoNiV is the most difficult alloy to embrittle because the reduction in surface energy with H is the lowest, while the γ^{usf} is smallest and increases most slowly with H.

Figure 4 summarizes all the experiments and theory predictions for all six alloys and Ni [59], ordered from most to least embrittled, showing the broad success of the theory in capturing the embrittlement transition concentration. The HEAs CoCrFeMnNi and CoCrFeNi are *not* fundamentally the most resistant to HE; SS316L is more resistant than both. The new CoNiV alloy is, however, even more resistant, with theory predicting embrittlement only beyond $C_b \sim 10\,000$ at. ppm. In general, the HEAs do not have unique embrittlement resistance simply due to compositional complexity. Embrittlement is far more subtle, depending on the effects of H on several different material properties. Note that physics dictates that embrittlement is determined by C_b, but experimental samples are often charged at an imposed chemical potential μ, and so different alloys charged at the same μ will have different H concentrations. This can shift the *apparent* embrittlement trends as compared to those based on the actual C_b in the alloy (see Sec. 7 in the Supplemental Material). The theory also suggests that the roles of H on influencing surrounding plasticity, twinning, H trapping at other defects, etc. are secondary phenomena; they may influence macroscopic toughness, change dislocation and deformation behaviors, and/or modulate the internal H concentration in the lattice, but they are not directly connected to the embrittlement process.

The theory enables a multistage approach to the computationally guided search and design of embrittlement resistant steels and HEAs (see Sec. 8 in the Supplemental Material). The present theory combined with the predictive theory for alloy yield strength [60] can further identify new steels alloys and HEAs that satisfy application requirements for strength and resistance to hydrogen embrittlement.

X. Z. and W. C. thank the Swiss National Science Foundation for support through the project “Harnessing atomic-scale randomness: design and optimization of mechanical performance in High Entropy Alloys” (Project No. 200021_118198/1).

---

[*] Corresponding author.
x.zhou@epfl.ch

[1] W. H. Johnson, Proc. R. Soc. **23**, 168 (1875).
[2] A. Turnbull, Testing and modelling for prediction of hydrogen embrittlement, in *Ageing Studies and Lifetime Extension of Materials*, edited by L. G. Mallinson (Springer US, Boston, MA, 2001), pp. 397–414.
[3] S. P. Lynch, Metall. Mater. Trans. A **44**, 1209 (2013).
[4] O. Barrera, D. Bombac, Y. Chen, T. Daff, E. Galindo-Nava, P. Gong, D. Haley, R. Horton, I. Katzarov, J. Kermode *et al.*, J. Mater. Sci. **53**, 6251 (2018).
[5] K. E. Nygren, K. Bertsch, S. Wang, H. Bei, A. Nagao, and I. Robertson, Curr. Opin. Solid State Mater. Sci. **22**, 1 (2018).
[6] K. E. Nygren, The influence of hydrogen on the evolving microstructure during fatigue crack growth in metastable and stable austenitic stainless steels, Ph.D. thesis, University of Illinois at Urbana-Champaign, 2016.
[7] K. M. Bertsch, S. Wang, A. Nagao, and I. M. Robertson, Mater. Sci. Eng.: A **760**, 58 (2019).
[8] Y. Zhao, D. Lee, M. Seok, J. Lee, M. Phaniraj, J. Suh, H. Ha, J. Kim, U. Ramamurty, and J. Jang, Scr. Mater. **135**, 54 (2017).
[9] Y. Zhao, D.-H. Lee, W.-J. Kim, M.-Y. Seok, J.-Y. Kim, H. N. Han, J.-Y. Suh, U. Ramamurty, and J.-i. Jang, Mater. Sci. Eng.: A **718**, 43 (2018).
[10] B. Gludovatz, A. Hohenwarter, D. Catoor, E. H. Chang, E. P. George, and R. O. Ritchie, Science **345**, 1153 (2014).
[11] A. L. Gurson, J. Eng. Mater. Technol. **99**, 2 (1977).
[12] E. Bitzek and P. Gumbsch, Acta Mater. **61**, 1394 (2013).
[13] T. Hajilou, Y. Deng, B. R. Rogne, N. Kheradmand, and A. Barnoush, Scr. Mater. **132**, 17 (2017).
[14] A. A. Griffith, Phil. Trans. R. Soc. A **221**, 163 (1921).
[15] J. R. Rice, J. Mech. Phys. Solids **40**, 239 (1992).
[16] P. Andric and W. Curtin, J. Mech. Phys. Solids **106**, 315 (2017).
[17] A. Tehranchi, X. Zhou, and W. Curtin, Acta Mater. **185**, 98 (2020).

[18] See Supplemental Material, which include Refs. [19–38], at http://link.aps.org/supplemental/10.1103/PhysRevLett.127.175501 for more details.

[19] G. Kresse and J. Furthmüller, Phys. Rev. B **54**, 11169 (1996).

[20] J. P. Perdew, K. Burke, and M. Ernzerhof, Phys. Rev. Lett. **77**, 3865 (1996).

[21] G. Kresse and D. Joubert, Phys. Rev. B **59**, 1758 (1999).

[22] P. E. Blöchl, Phys. Rev. B **50**, 17953 (1994).

[23] M. Methfessel and A. T. Paxton, Phys. Rev. B **40**, 3616 (1989).

[24] H. J. Monkhorst and J. D. Pack, Phys. Rev. B **13**, 5188 (1976).

[25] A. van de Walle and G. Ceder, J. Phase Equilib. **23**, 348 (2002).

[26] A. Van De Walle, CALPHAD: Comput. Coupling Phase Diagrams Thermochem. **33**, 266 (2009).

[27] X. Zhou and W. A. Curtin, Acta Mater. **200**, 932 (2020).

[28] M. ed Levy, E. Henry, R. Richard, and V. Keppens, *Handbook of Elastic Properties of Solids, liquids, and Gasses Vol. 3: elastic Properties of Solids: biological and Organic Materials, earth and Marine Sciences* (Academic Press, New York, 2001), Vol. 3.

[29] T. Teramoto, K. Yamada, R. Ito, and K. Tanaka, J. Alloys Compd. **777**, 1313 (2019).

[30] A. Teklu, H. Ledbetter, S. Kim, L. Boatner, M. McGuire, and V. Keppens, Metall. Mater. Trans. A **35**, 3149 (2004).

[31] B. Yin, S. Yoshida, N. Tsuji, and W. Curtin, Nat. Commun. **11**, 1 (2020).

[32] S. Plimpton, J. Comput. Phys. **117**, 1 (1995).

[33] Y. Fukai, J. Less-Common Met. **172**, 8 (1991).

[34] Y. Mishin, D. Farkas, M. Mehl, and D. Papaconstantopoulos, Phys. Rev. B **59**, 3393 (1999).

[35] G. Henkelman, B. P. Uberuaga, and H. Jónsson, J. Chem. Phys. **113**, 9901 (2000).

[36] T. Matsuo, J. Yamabe, and S. Matsuoka, Int. J. Hydrogen Energy **39**, 3542 (2014).

[37] Y. Kim, Y. Kim, D. Kim, S. Kim, W. Nam, and H. Choe, Mater. Trans., JIM **52**, 507 (2011).

[38] C. San Marchi, T. Michler, K. Nibur, and B. Somerday, Int. J. Hydrogen Energy **35**, 9736 (2010).

[39] J. Song, M. Soare, and W. Curtin, Model. Simul. Mater. Sci. Eng. **18**, 045003 (2010).

[40] J. Song and W. Curtin, Nat. Mater. **12**, 145 (2013).

[41] S. S. Shishvan, G. Csányi, and V. S. Deshpande, J. Mech. Phys. Solids **134**, 103740 (2020).

[42] H. Vehoff and W. Rothe, in *Perspectives in Hydrogen in Metals*, edited by M. F. Ashby and J. P. Hirth (Pergamon Press, 1986), pp. 647–659, https://doi.org/10.1016/B978-0-08-034813-1.50091-7.

[43] G. R. Caskey Jr, Hydrogen compatibility handbook for stainless steels, Technical Report No. DP-1643-DE83017051, Du Pont de Nemours (EI) and Co., Aiken, SC (USA), Savannah River Lab., 1983.

[44] G. Caskey Jr, Fractography of hydrogen-embrittled stainless steel, Technical Report No. DP-MS-76-65, Du Pont de Nemours (EI) and Co., Aiken, SC (USA), Savannah River Lab., 1977.

[45] G. R. Caskey Jr, Hydrogen damage in stainless steel, Technical Report No. DP-MS-81-31, Du Pont de Nemours (EI) and Co., Aiken, SC (United States), Savannah River Lab., 1981.

[46] M. Hatano, M. Fujinami, K. Arai, H. Fujii, and M. Nagumo, Acta Mater. **67**, 342 (2014).

[47] Y. Wang, X. Wu, X. Li, W. Wu, and J. Gong, Int. J. Hydrogen Energy **44**, 7014 (2019).

[48] L. Zhang, Z. Li, J. Zheng, Y. Zhao, P. Xu, C. Zhou, C. Zhou, and X. Chen, Int. J. Hydrogen Energy **39**, 20578 (2014).

[49] C. San Marchi, B. Somerday, X. Tang, and G. Schiroky, Int. J. Hydrogen Energy **33**, 889 (2008).

[50] Y. Mine and T. Kimoto, Corros. Sci. **53**, 2619 (2011).

[51] M. Koyama, K. Ichii, and K. Tsuzaki, Int. J. Hydrogen Energy **44**, 17163 (2019).

[52] K. Ichii, M. Koyama, C. C. Tasan, and K. Tsuzaki, Scr. Mater. **150**, 74 (2018).

[53] H. Luo, Z. Li, and D. Raabe, Sci. Rep. **7**, 1 (2017).

[54] K. E. Nygren, S. Wang, K. M. Bertsch, H. Bei, A. Nagao, and I. M. Robertson, Acta Mater. **157**, 218 (2018).

[55] M. Koyama, H. Wang, V. K. Verma, K. Tsuzaki, and E. Akiyama, Metall. Mater. Trans. A **51**, 5612 (2020).

[56] J. Yi, X. Zhuang, J. He, M. He, W. Liu, and S. Wang, Corros. Sci. **189**, 109628 (2021).

[57] C. K. Soundararajan, H. Luo, D. Raabe, and Z. Li, Corros. Sci. **167**, 108510 (2020).

[58] H. Luo, S. S. Sohn, W. Lu, L. Li, X. Li, C. K. Soundararajan, W. Krieger, Z. Li, and D. Raabe, Nat. Commun. **11**, 1 (2020).

[59] K. Wada, J. Yamabe, and H. Matsunaga, Materialia **8**, 100478 (2019).

[60] C. Varvenne, A. Luque, and W. A. Curtin, Acta Mater. **118**, 164 (2016).